Communication

A Parallel Folded Dipole Antenna With an Enhanced Bandwidth for 5G Millimeter-Wave Applications

Qingquan Tan, Kuikui Fan, Weiliang Yu, Leilei Liu, and Guo Qing Luo

***Abstract*— In this communication, a planar folded dipole antenna array with wide operating bandwidth and compact size is proposed for 5G millimeter-wave (mmWave) applications. The basic antenna element is a pair of parallel folded dipoles (PFDs) connected at the terminals. Compared with a single half-wavelength dipole, the PFD can achieve a flatter impedance curve in the working frequency band, and it is easier to achieve broadband impedance matching with 50-Ω feeding line. Moreover, a coupling slot feeding method is adopted to feed the proposed antenna element. The capacitance provided by the coupling slot can counteract the inductance caused by the PFD, thus improving the impedance matching at the low-frequency band. Benefiting from the innovative design, the proposed antenna element can achieve an ultra-wide impedance bandwidth of 64% and a compact size of $0.26\lambda_0 \times 0.28\lambda_0$. Furthermore, a wide scanning angle with ±50° over wide bandwidth is testified by a 1 × 8 array using active simulation. For verification, a 4 × 4 full corporate-fed array is designed based on the proposed element. The measured results prove that the proposed 4 × 4 array has a −10 dB impedance bandwidth of 65% covering 17–33.75 GHz and a peak gain of 17.5 dBi. The measured total efficiency is from 69% to 82% over the working frequency band. With the merits of compact size, wide working bandwidth, and wide beam scanning angle, the proposed antenna is a good candidate for mmWave wireless communications.**

***Index Terms*— Antenna array, millimeter wave (mmWave), parallel folded dipoles (PFDs), wide scan angle, wideband antenna.**

I. Introduction

With the demand for high capacity, high speed, and low latency, modern communication frequencies will inevitably extend to millimeter-wave (mmWave) bands. The N257 (26.5–29.5 GHz), N258 (24.25–27.5 GHz), N259 (39.5–43.5 GHz), and N260 (37–40 GHz) bands were licensed for 5G mmWave communication [1], in which most countries are deploying 5G mmWave across the 24.25–29.5 GHz range. To provide good compatibility, wireless systems need to cover as many bands as possible. Therefore, it is desirable to design the mmWave antenna working at a wide frequency range or multibands. In addition, the mmWave spectrum suffers from a limited propagation distance due to high-propagation attenuation, which requires high-gain antenna arrays. Also with mmWave, beam scanning is critical to identify the direction of interest. Hence, as a key component for wireless communications, it is meaningful to design mmWave antennas with wide bandwidth, high gain, and wide scanning range.

Various types of broadband mmWave antennas and arrays have been developed in recent years. Due to the high dielectric loss of substrates at mmWave, hollow waveguide-fed metal antennas [2], [3], [4], [5] and gap waveguide-fed metal antennas [6], [7], [8], [9] were developed to achieve high gain and high efficiency. A Ka-band magnetoelectric (ME) dipole array fed by the waveguide was presented in [2] using 3-D printed technology. A bandwidth of 31%, a maximum gain of 28.5 dBi, and a radiation efficiency of about 90% were obtained. Considering that the bandwidths of previous full-metal arrays were less than 40%, a wideband full-metal planar array with gap waveguide technology was proposed in [9] and achieved an impedance bandwidth of 48% and a maximum gain of 27 dBi. However, the metal antennas suffer from a bulky volume and integration difficulty, which is undesirable for lightweight and highly integrated equipment.

Despite the existence of relatively high dielectric loss, the planar antennas based on printed circuit board (PCB) are still popular in the mmWave band owing to lightweight, small volume, high integration, and ease of mass production. Many PCB-based antennas and arrays had been implemented in the mmWave band [10], [11], [12], [13], [14], [15], [16], [17], [18], [19], [20], [21], [22], [23], [24], [25], [26], [27], [28], [29], [30]. Researchers had made many efforts to expand the bandwidth of the mmWave antennas. Several wideband antenna arrays were proposed in [10], [11], [12], [13], [14], and [15], but their working bandwidths were still less than 25%. Different types of antennas and arrays with bandwidth greater than 35% were proposed in [16], [17], [18], [19], [20], [21], [22], [23], [24], [25], [26], [27], [28], [29], and [30], such as E-patch antennas [16], [17], bowtie dipole [18], C-shaped slot antenna [19], dipoles with parasitic patches [20], [21], metasurface antennas [22], [23], and ME-dipole antennas [24], [25], [26], [27], [28], [29], [30]. The symmetrical E-shaped patch antenna [17] and C-shaped slot antenna [19] have large sizes. In [16], [20], and [21], the back cavities used to suppress the surface wave result in a large size of antennas. Therefore, they are not suitable for beam scanning applications. ME-dipole antennas [24], [25], [26], [27], [28], [29], [30] feature wide working bandwidth of over 40%, compact size, and stable radiation patterns. Hence, they were attractive for wideband or multibeam systems. A miniaturized ME-dipole antenna was presented in [26] by etching transverse slots on the electric dipole. This ME-dipole antenna achieved a bandwidth of 48% and the scanning angle of ±45° over a wide band was verified by a 1 × 8 array with active simulation.

Manuscript received 14 December 2022; revised 31 March 2023; accepted 9 April 2023. Date of publication 14 June 2023; date of current version 4 August 2023. This work was supported in part by the National Natural Science Foundation of China under Grant 62271183, Grant 62125105, and Grant 62001250; in part by the "Pioneer" and "Leading Goose" Research and Development Program of Zhejiang under Grant 2022C01231 and Grant 2022C01119; and in part by the Open Fund of the State Key Laboratory of Millimeter Waves of China under Grant K202329 and Grant K202308. *(Corresponding author: Kuikui Fan.)*

Qingquan Tan and Guo Qing Luo are with the Key Laboratory of RF Circuits and Systems, Ministry of Education, School of Electronics and Information, Hangzhou Dianzi University, Hangzhou 310018, China (e-mail: luoguoqing@hdu.edu.cn).

Kuikui Fan and Weiliang Yu are with the Key Laboratory of RF Circuits and Systems, Ministry of Education, School of Electronics and Information, Hangzhou Dianzi University, Hangzhou 310018, China, and also with the State Key Laboratory of Millimeter Waves, Southeast University, Nanjing 211189, China (e-mail: kkfan@hdu.edu.cn).

Leilei Liu is with the National and Local Joint Engineering Laboratory of RF Integration, College of Electronic and Optical Engineering, Nanjing University of Posts and Telecommunications, Nanjing 210003, China (e-mail: liull@njupt.edu.cn).

Color versions of one or more figures in this communication are available at https://doi.org/10.1109/TAP.2023.3277189.

Digital Object Identifier 10.1109/TAP.2023.3277189

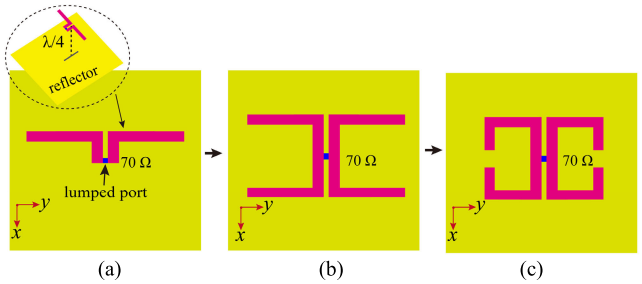

Fig. 1. Evolution of PFD. (a) Half-wavelength dipole. (b) Parallel dipole. (c) PFD.

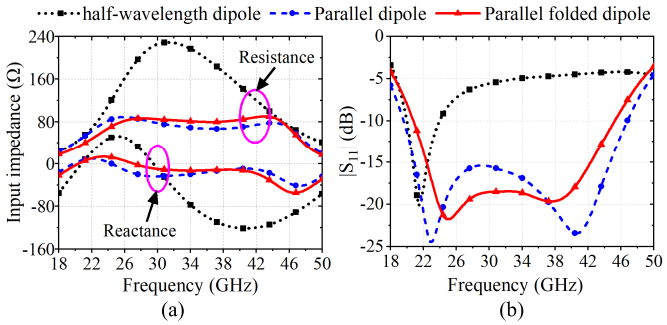

Fig. 2. Simulated results of three antennas. (a) Input impedance. (b) Reflection coefficient.

A broadband antenna consisting of a pair of folded dipoles connected in parallel was proposed in [31] for 2G/3G/LTE base stations. However, the overall layout and feed way are difficult to directly implement in mmWave. Inspired by this work, a wideband parallel folded dipole (PFD) antenna is proposed in this communication. A simple feeding method is constructed by a coupling slot and two grounded metal vias. The two grounded metal vias are located on both sides of the coupling slot to differentially excite the PFD antenna. The proposed antenna exhibits wide bandwidth, compact size, wide scanning angle, and high integration. For verification, a 4×4 full corporate-fed array achieves a -10 impedance bandwidth of 65% covering 17–33.75 GHz.

II. Design Concept

Before presenting the proposed antenna, the design concept of the parallel dipole is studied as the basis of the proposed antenna. First, the broadband characteristics of the parallel dipole are demonstrated in free space. Then, as the theoretical support, the input impedance of the parallel dipole is deduced by building an equivalent model.

A. Evolution and Performance of PFD

Fig. 1 shows the evolution process of the PFD. These three antennas are fed by a lumped port in HFSS. The simulated input impedance and reflection coefficient are given in Fig. 2. First, a half-wavelength dipole is placed above the metal reflector in free space and the height from the half-wavelength dipole to the reflector is a quarter of wavelength. It can be seen from Fig. 2(a) that the half-wavelength dipole has very high input resistances in the high-frequency band. Therefore, it is difficult to achieve wide working bandwidth for the half-wavelength dipole. To reduce resistance, two half-wavelength dipoles are connected in parallel, which forms a parallel dipole. From Fig. 2(a), the input resistance of the parallel dipole is significantly reduced compared with the half-wavelength dipole, and a flat input resistance curve near 75 Ω can be observed between the two resistance peaks. Meanwhile, the input reactance of the parallel dipole changes smoothly around 0. The input impedance of the parallel dipole will be derived in Section II-B. From Fig. 2(b),

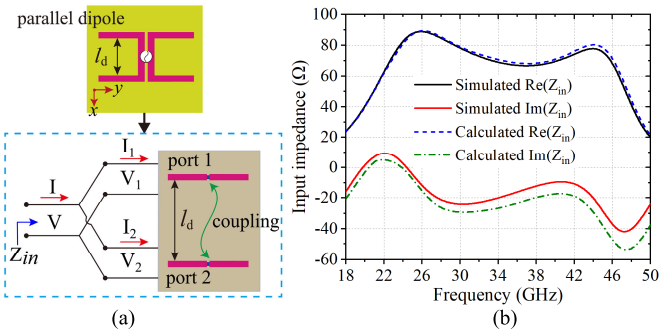

Fig. 3. (a) Equivalent circuit model of the parallel dipole. (b) Simulated and calculated the input impedance of the parallel dipole.

the parallel dipole exhibits a wide impedance bandwidth of approaching 80% at a defined port impedance of 70 Ω. Furthermore, the terminals of the parallel dipole are bent inward to construct a PFD, which can effectively reduce the footprint of the parallel dipole. It can be seen from Fig. 2(a) that the bending terminals have only a slight effect on the input impedance, but the length in the y-direction is reduced by 20%. The PFD features a wideband band and compact size, which is attractive for wideband array and wide-angle scanning.

B. Equivalent Model of the Parallel Dipole

Section II-A shows that the parallel dipole has a flat input resistance and reactance curve over a wide frequency band, which is mainly attributed to two factors: 1) a pair of dipoles are connected in parallel, reducing the input resistance and smoothing the input reactance and 2) the parallel dipole can be viewed as an antenna array with two closely spaced elements. Hence, tight coupling between elements can help to improve impedance matching. As an explanation, an equivalent model is shown in Fig. 3(a). The parallel dipole can be decomposed into two dipoles excited by a common mode signal. The relationship between voltage and current at port 1 and port 2 can be conveniently expressed using an impedance matrix

$$\begin{bmatrix} V_1 \\ V_2 \end{bmatrix} = \begin{bmatrix} Z_{11} & Z_{12} \\ Z_{21} & Z_{22} \end{bmatrix} \begin{bmatrix} I_1 \\ I_2 \end{bmatrix}. \tag{1}$$

According to (1), the common-mode impedance Z_{cm} can be expressed as

$$V_{cm} = V_1 + V_2 \tag{2}$$

$$I_{cm} = I_1 = I_2 \tag{3}$$

$$Z_{cm} = \frac{V_{cm}}{I_{cm}} = Z_{11} + Z_{12} + Z_{21} + Z_{22}. \tag{4}$$

Considering that port 1 and port 2 are connected in parallel, additional conditions should be satisfied

$$V_1 = V_2 = V \tag{5}$$

$$I_1 = I_2 = \frac{I}{2}. \tag{6}$$

According to (2)–(6) and considering network reciprocity, the input impedance Z_{in} of the parallel dipole can be derived

$$Z_{in} = \frac{V}{I} = \frac{1}{4}(Z_{11} + Z_{12} + Z_{21} + Z_{22}) \quad = \frac{1}{2}(Z_{11} + Z_{12}). \tag{7}$$

It is clear from (7) that the input impedance of the parallel dipole is affected by its self-impedance as well as the mutual impedance. For validation, two dipoles fed by lumped ports are constructed in the HFSS to extract the Z-parameters. Fig. 3(b) shows the simulated and calculated input impedance of the parallel dipole. It can be observed that the two curves agree well. The slight difference comes from the unequal length of feeding strips. This verifies the correctness of (7).

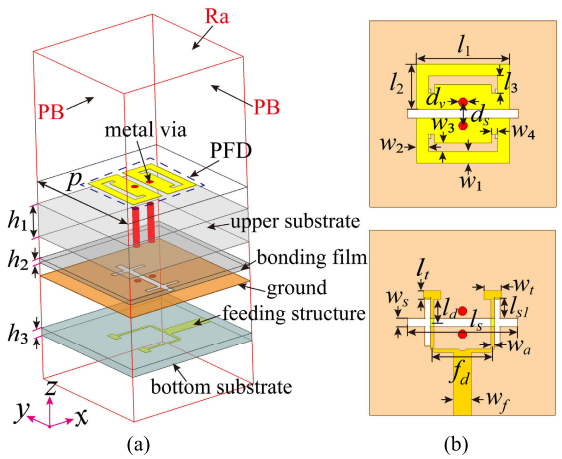

Fig. 4. Geometry of the proposed PFD antenna based on PCB. (a) 3-D view. (b) Top view. Parameters (unit: mm): $p = 6.4$, $w_1 = 0.4$, $w_2 = 0.42$, $w_3 = 0.3$, $w_4 = 0.2$, $l_1 = 3.2$, $l_2 = 1.55$, $l_3 = 0.6$, $d_v = 0.3$, $d_s = 0.7$, $w_s = 0.3$, $l_s = 3.8$, $l_{s1} = 0.7$, $w_t = 0.6$, $l_t = 0.3$, $l_d = 0.8$, $w_a = 0.12$, f_d =2.1, $w_f = 0.6$, $h_1 = 1.52$, $h_2 = 0.1$, and $h_3 = 0.25$. (PB: periodic boundary and Ra: radiation boundary).

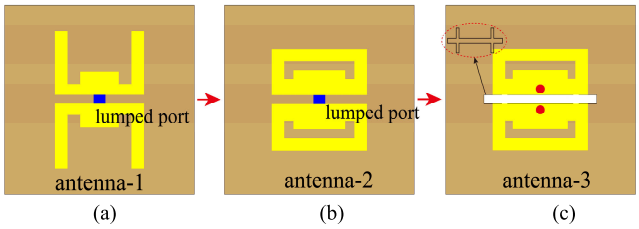

Fig. 5. Evolution of the proposed PCB-based PFD. (a) Parallel dipole. (b) PFD. (c) Final design.

By adjusting spacing l_d to change mutual impedance Z_{12}, a flatter impedance curve can be achieved for wideband impedance matching.

III. Antenna Design And Analysis

In Section II, the PFD demonstrates the potential for wide working bandwidth and compact size. Based on this design concept, a planar PCB-based PFD antenna will be developed in this section.

A. Configuration and Performance of the Proposed PFD

The whole layout of the proposed PFD is illustrated in Fig. 4, including two substrates (i.e., top and bottom substrates) and three copper layers. The two substrates are RO3003 ($\varepsilon_r = 3$ and $\tan\delta = 0.0013$) and bonded together by a bonding film Rogers 4450F with a thickness of 0.1 mm ($\varepsilon_r = 3.5$ and $\tan\delta = 0.004$). The thickness of the top substrate is 1.52 mm, and the total height of the top substrate and bonding film corresponds to a $\lambda_g/4$ at 25 GHz. (λ_g is the dielectric wavelength.) The PFD antenna is printed on the upper substrate. Two symmetrical metal vias connect the PFD antenna to the ground. A like H-shaped slot is cut on the ground to differentially feed the PFD antenna through the two metal vias. Compared with a routine H-coupling slot, the like H-shaped slot is more flexible for adjusting impedance matching. Then, a feed structure based on a T-junction power divider is printed on the bottom substrate. For designing a fixed beam array, the proposed PFD antenna is directly optimized under periodic boundaries (PBs) to take into account the effect of mutual coupling on the reflection coefficient. The element spacing is selected to be about $0.7\lambda_{upper}$ to obtain more space for the feeding network. The final design dimensions of the proposed antenna are also given in Fig. 4.

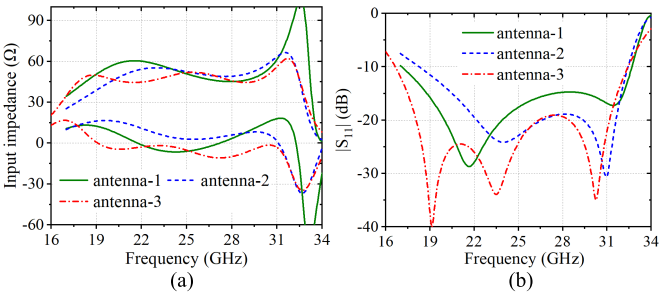

Fig. 6. Simulated results of these three antennas. (a) Input impedance. (b) Reflection coefficient.

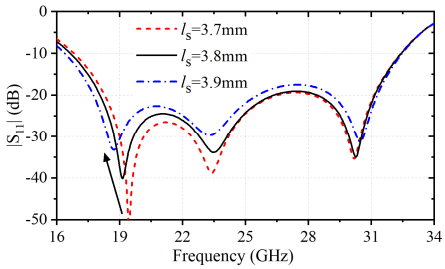

Fig. 7. Simulated reflection coefficient of the proposed antenna with a different coupling slot length l_s.

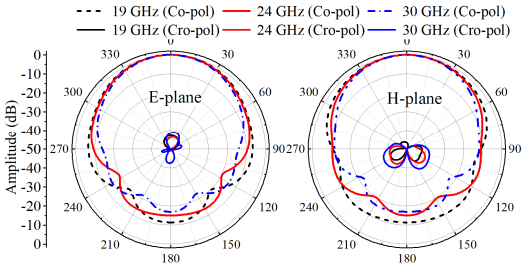

Fig. 8. Radiation patterns of the proposed PFD antenna at three frequencies.

Fig. 5 shows the evolution process of the proposed PCB-based PFD antenna. The design starts with a parallel dipole. A pair of rectangular patches attached to the center are used for fine-tuning impedance matching. Then, the terminals of the parallel dipole are bent inward to reduce the antenna footprint. For practical applications, a slot coupling method is adopted to replace the lumped port. Fig. 6 shows the input impedance and $|S_{11}|$ of these three antennas. The PCB-based PFD fed by a lumped port has the smooth impedance curve with weak inductive reactance and can provide a wide working bandwidth of 54% covering 18.5–32.4 GHz. Then, using the coupling slot as excitation, the introduced capacitance can effectively compensate for inductance, which produces an additional resonance at 19 GHz. Fig. 7 reveals the influence of coupling slot length l_s on $|S_{11}|$ of the proposed PFD antenna. As the l_s increases, the first resonant frequency moves toward a lower frequency, while the other resonances are almost unaffected. The additional resonance helps to improve impedance matching in the lower band and broadens the antenna bandwidth. Benefitting the broadband property of the parallel dipole, the proposed antenna realizes an impedance bandwidth of 64% from 16.7 to 32.5 GHz, about a one-octave band. Fig. 8 shows the radiation patterns of the proposed antenna at three resonant frequencies. It shows that the proposed PFD exhibits high stability in both radiation patterns and cross-polarization levels, with the latter below −40 dB.

Fig. 9 shows the surface currents of the proposed PFD at three resonant frequencies. Similar current distributions at three frequencies can be observed. The current flows along the bent arms and is guided to the ground by two metallic vias. The zero currents at the

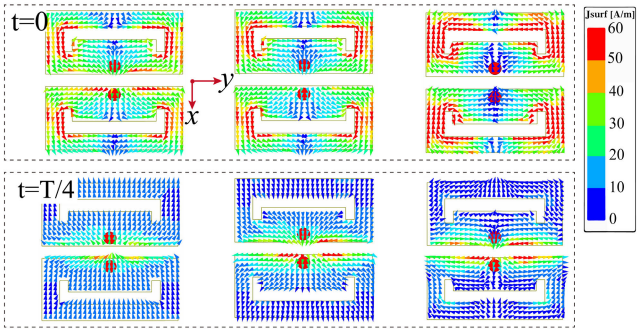

Fig. 9. Surface currents of the proposed PFD at different times. (a) 19 GHz. (b) 24 Hz. (c) 30 GHz.

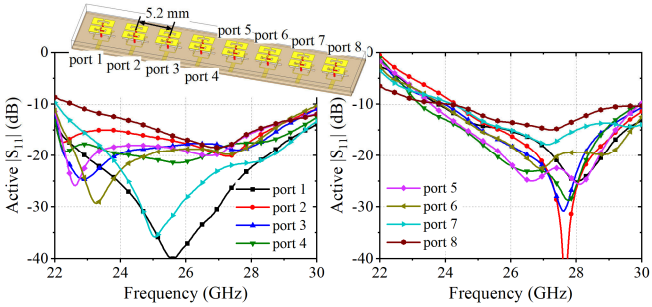

Fig. 10. Active reflection coefficients of eight elements at different scanning angles. (a) 25°. (b) 50°.

center position can be clearly seen. The resultant currents at three frequencies are along the x-direction, while the horizontal currents in the y-direction always cancel each other out, which results in low cross-polarization levels. The current distribution verifies that the proposed antenna is a pair of folded dipoles connected in parallel.

B. Beam Scanning Verification

Beam scanning is an important requirement for mmWave wireless systems. The beam scanning performance of the proposed PFD is investigated in this section. Active simulation is applied to a 1 × 8 array to validate the beam scanning capability. The element spacing is set to about $0.5\lambda_0$ at 29 GHz to obtain wide scanning angles. Due to the change of field environments, the proposed PFD antenna has been re-optimized and the folded terminals are no longer connected together to suppress parasitic modes that occur in the large scanning angle. Fig. 10 shows the active reflection coefficient at different scanning angles. The scanning angle is calculated at 26 GHz. It can be seen that the active $|S_{11}|$ of each element can approximately cover the N258 (24.25–27.5 GHz) and N257 (26.5–29.5 GHz) bands of 5G mmWave even if the scanning angle is up to 50°. Fig. 11 exhibits the simulated scanning patterns at 24, 26, 28, and 30 GHz. It can be seen that the scanning angles can reach ±50° at all four frequencies. The scanning losses at 24, 26, 28, and 30 GHz are 1, 1.2, 1.5, and 2.6 dB, respectively. The sidelobe levels at the four frequencies are lower than −10 dB. This verifies that the proposed antenna has excellent scanning capability.

IV. Antenna Array

For mmWave wireless communication, a high-gain array antenna is necessary to ensure the link budget. As shown in Fig. 12, the designed PFD antenna is expanded to a full corporate-fed 4 × 4 array by using a simple microstrip feeding network. Antenna elements are located on the top substrate and arranged at intervals of 6.4 mm in both the x- and y-directions, which is corresponding to about

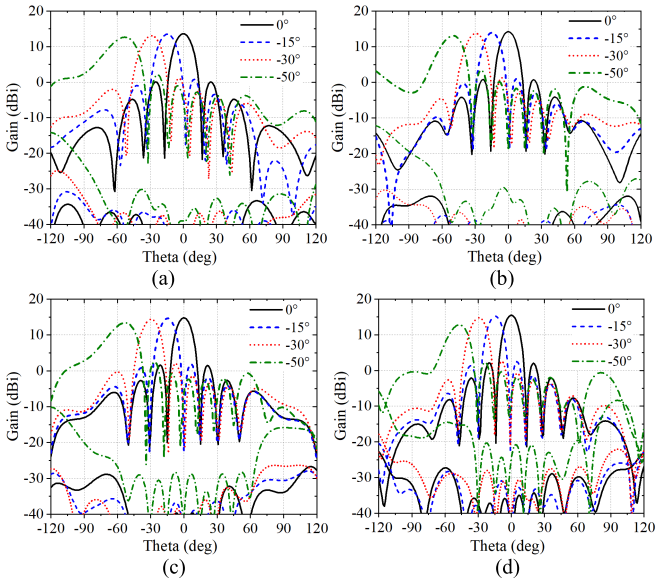

Fig. 11. Simulated radiation patterns of the designed 1 × 8 antenna array with different scanning angles in the *yoz* plane. (a) 24 GHz. (b) 26 GHz. (c) 28 GHz. (d) 30 GHz.

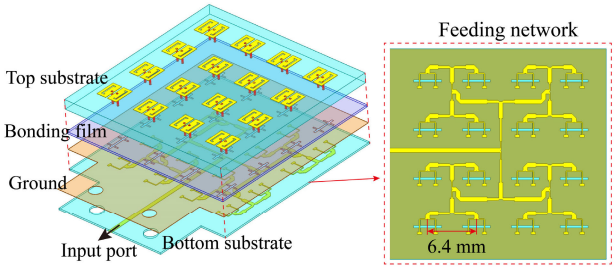

Fig. 12. Geometry of the proposed 4 × 4 antenna array.

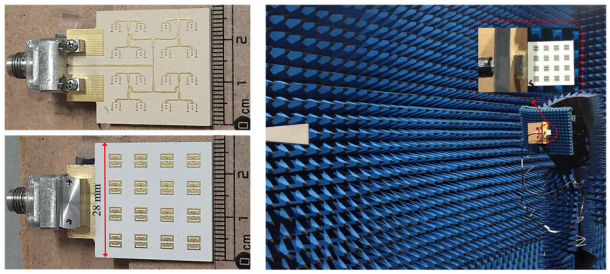

Fig. 13. Photographs of (a) fabricated 4 × 4 antenna array and (b) test scenario in the far-field anechoic chamber.

$0.7\lambda_0$ at 33 GHz. The microstrip feeding network is integrated into the bottom substrate to excite elements with the same amplitudes and phases. It is noted that the T-shaped part of the feeding line is slightly adjusted to maintain good impedance matching. To facilitate testing, an extension substrate is added to the input port so that a coaxial connector can be connected. Two Rogers Ro3003 substrates are stacked together by a 0.1-mm-thick bonding film. A standard multilayer PCB manufacturing process is adopted to fabricate the antenna array.

V. Results and Discussion

The measurement results of the proposed array and a comparison with the reported mmWave array will be described in this section.

A. Prototype and Experimental Results

To certify the performance of the array, a prototype of the designed 4 × 4 antenna array was machined. The antenna array

TABLE I
PERFORMANCE COMPARISON WITH REPORTED PLANAR LINEAR POLARIZED ARRAYS

Ref.	Element type	ε_r / tan(δ)	No. of substrate layer*	No. of elements	Center Freq. (GHz)	Element Size (λ_c^2)	Imp. BW (%)	Max. gain (dBi)	Antenna Efficiency (%)	Overall profile (mm)
[16]	E-patch	2.2/0.0009	1	2×2	45	0.8×0.58	34.4	12.5	60~88	0.50(0.076λ_c)
[18]	Bowtie dipole	3.0/0.0011	4	8×8	25	0.46×0.44	50.3	22.1	40~75	4.06/(0.34λ_c)
[19]	C-open slot	2.2/0.0009	2	8×8	26	1.13×0.76	37.1	28.3	70.1	3.14/(0.27λ_c)
[20]	Dipole patch	2.2/0.0009	2	8×8	27	0.81×0.81	23	25.5	N.A	1.56/(0.14λ_c)
[23]	Metasurface	2.2/0.0009	3	4×4	34	0.43×0.43	35.5	17.4	60~80 (sim.)	2.55/(0.29λ_c)
[26]	ME-dipole	2.2/0.0009	2	1×16	35	0.51×0.54	57	19	62~85 (sim.)	1.14/(0.13λ_c)
[27]	ME-dipole	2.2/0.0009	2	4×4	28	0.56×0.49	44.6	19.2	>85%*	1.73/(0.16λ_c)
[28]	ME-dipole	2.2/0.0009	4	4×4	32	0.47×0.47	51.5	20.3	85%*	2.68/(0.28λ_c)
[29]	ME-dipole	3.5/0.0015	3	1×8	32	0.27×0.35	49	14.7	60~91	1.24/(0.13λ_c)
[30]	ME-dipole	3.66/0.0037	3	1×4	32	0.22×0.35	48	12.65	60~80	1.26/(0.13λ_c)
This work	Parallel folded dipole	3.0/0.0013	2	4×4	25	0.26×0.28	65	17.5	69~82	1.85/(0.15λ_c)

*: simulated radiation efficiency.

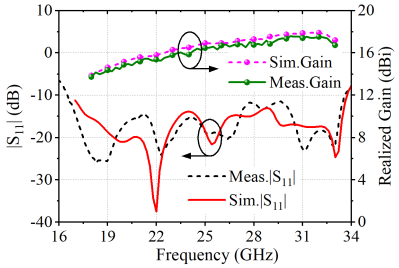

Fig. 14. Measured and simulated results of the proposed 4 × 4 array, including $|S_{11}|$ and gain.

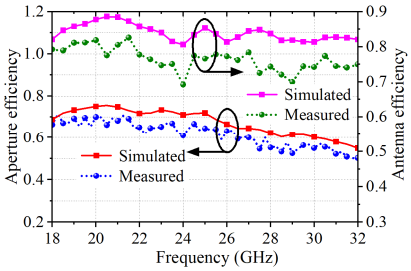

Fig. 15. Measured and simulated results of the proposed 4 × 4 array, including aperture efficiency and antenna efficiency.

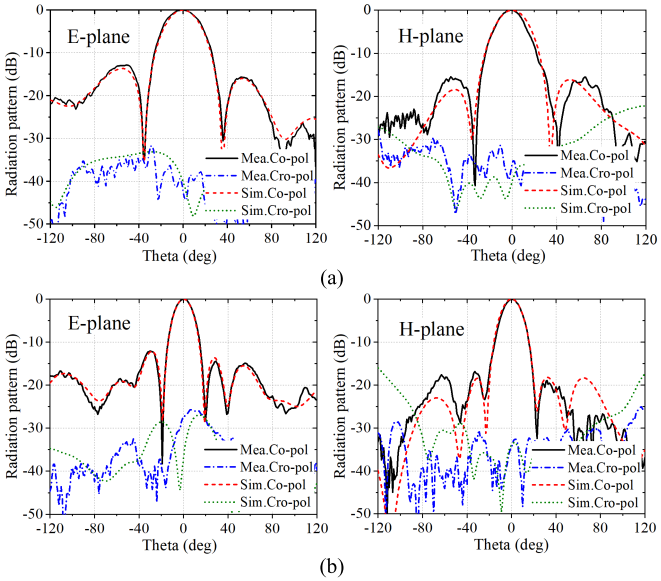

Fig. 16. Simulated and measured radiation patterns of the proposed 4 × 4 array. (a) 20 GHz. (b) 32 GHz.

occupies an area of 28 × 28 mm^2. Fig. 13(a) shows the photograph of the machined array prototype. To create a good electrical contact, the bottom substrate is extended. The reflection coefficient of the machined array prototype is obtained by an Agilent Vector Network Analyzer N5245A. The simulated and measured reflection coefficients are given in Fig. 14. The measured impedance bandwidth of $|S_{11}| < -10$ dB is 65% covering 17–33.5 GHz and the measured $|S_{11}|$ is in good agreement with the simulated one. Then, the radiation performance of the 4 × 4 array is measured in a far-field anechoic chamber. The test scenario of the 4 × 4 array in the far-field anechoic chamber is manifested in Fig. 13(b). The measured gains are also given in Fig. 14. It indicates that the measured gain is from 13.7 and 17.5 dBi in the range of 18–33 GHz, while the simulated gain gains are in the range of 14.2–17.9 dBi. The simulated gains are on average 0.41 dB higher than the measured values. Reasons for the discrepancy include measurement inaccuracy, the loss of a feeding network, and increased material loss at mmWave. In addition, the antenna efficiencies and aperture efficiencies are given in Fig. 15. The simulated directivity is used to calculate the measured antenna efficiency which includes impedance mismatch efficiency and radiation efficiency. It can be seen that the proposed 4 × 4 antenna array has an antenna efficiency higher than 69% and an aperture efficiency higher than 50%. Due to lower measurement gains compared with simulated values, the measured antenna efficiency is also lower than the simulated result. Fig. 16 presents the simulated and measured radiation patterns at 20 and 32 GHz. A good consistency between measured and simulated patterns can be observed. Slight differences arise from manufacturing errors, misalignment during testing, and multipath reflection from the metallic bracket. The measured patterns show sidelobe levels below −13 dB and cross-polarization levels below −25 dB, respectively. The proposed 4 × 4 antenna array exhibits good radiation performance across its operating bandwidth.

B. Comparison and Discussion

Table I lists a comparison of performance between the proposed antenna array and several state-of-the-art mmWave antenna arrays. The antennas designed in [16] and [20] have a large size of over 0.8λ_c, which will limit their application in beam scanning. In [19], the antenna array achieves a high gain, but more than one wavelength intervals lead to grating lobes. In [18] and [28], four layers of substrates are used to design the array, which leads to a high profile and

increase fabrication cost. In [26], the ME-dipole is designed for endfire radiation, resulting in a complex 3-D structure. In [29] and [30], the sizes of the antennas are comparable with our work, but more substrates will increase manufacturing complexity. To sum up, this comparison confirms that the proposed array has the widest working bandwidth, a more compact size, acceptable antenna efficiency, and a relatively low profile.

VI. Conclusion

A wideband planar PFD antenna is presented and validated in this communication. First, the wideband characteristic of the parallel dipole in free space is confirmed, and its input impedance is derived as theoretical support. To obtain a more compact size, a PFD is designed by bending the dipole arms inward. Based on this design concept, a PCB-based planar PFD is designed by adopting the aperture-coupled method. The proposed PFD antenna features a wide bandwidth of 64% and a compact size of $0.26\lambda_0\times\ 0.28\lambda_0$. Meanwhile, a $1\ \times\ 8$ antenna array using active simulation reveals a wide scanning angle (up to $\pm\ 50°$) over the N257 and N258 bands. For experimental validation, a $4\ \times\ 4$ full corporate-fed array is constructed and tested. The measured results illustrate that the proposed $4\ \times\ 4$ array achieves a working bandwidth of 65% and an antenna efficiency higher than 69%. Good radiation performance and low cross-polarization levels are obtained under the whole working frequency band. The proposed PFD antenna exhibits good prospects for 5G mmWave application.

References

[1] W. Hong et al., "The role of millimeter-wave technologies in 5G/6G wireless communications," *IEEE J. Microw.*, vol. 1, no. 1, pp. 101–122, Jan. 2021.

[2] Y. Li et al., "A Ka-band 3-D-printed wideband stepped waveguide-fed magnetoelectric dipole antenna array," *IEEE Trans. Antennas Propag.*, vol. 68, no. 4, pp. 2724–2735, Apr. 2020.

[3] K. Fan, Z. C. Hao, Q. Yuan, G. Q. Luo, and W. Hong, "A wideband high-gain planar integrated antenna array for E-band backhaul applications," *IEEE Trans. Antennas Propag.*, vol. 68, no. 3, pp. 2138–2147, Mar. 2020.

[4] H. Zhao et al., "E-band full corporate-feed 32×32 slot array antenna with simplified assembly," *IEEE Antennas Wireless Propag. Lett.*, vol. 20, no. 4, pp. 518–522, Apr. 2021.

[5] P. Liu, G. F. Pedersen, and S. Zhang, "Wideband slot array antenna fed by open-ended rectangular waveguide at W-band," *IEEE Antennas Wireless Propag. Lett.*, vol. 21, no. 4, pp. 666–670, Apr. 2022.

[6] A. Farahbakhsh, D. Zarifi, and A. U. Zaman, "A mmWave wideband slot array antenna based on ridge gap waveguide with 30% bandwidth," *IEEE Trans. Antennas Propag.*, vol. 66, no. 2, pp. 1008–1013, Feb. 2018.

[7] W. Y. Yong, A. Haddadi, T. Emanuelsson, and A. A. Glazunov, "A bandwidth-enhanced cavity-backed slot array antenna for mmWave fixed-beam applications," *IEEE Antennas Wireless Propag. Lett.*, vol. 19, no. 11, pp. 1924–1928, Nov. 2020.

[8] L. Zhang et al., "Wideband 45° linearly polarized slot array antenna based on gap waveguide technology for 5G millimeter-wave applications," *IEEE Antennas Wireless Propag. Lett.*, vol. 20, no. 7, pp. 1259–1263, Jul. 2021.

[9] T. Zhang, R. Tang, L. Chen, S. Yang, X. Liu, and J. Yang, "Ultra-wideband full-metal planar array antenna with a combination of ridge gap waveguide and E-plane groove gap waveguide," *IEEE Trans. Antennas Propag.*, vol. 70, no. 9, pp. 8051–8058, Sep. 2022.

[10] M. Li and K. Luk, "Low-cost wideband microstrip antenna array for 60-GHz applications," *IEEE Trans. Antennas Propag.*, vol. 62, no. 6, pp. 3012–3018, Jun. 2014.

[11] Q. Zhu, K. B. Ng, C. H. Chan, and K. Luk, "Substrate-integrated-waveguide-fed array antenna covering 57–71 GHz band for 5G applications," *IEEE Trans. Antennas Propag.*, vol. 65, no. 12, pp. 6298–6306, Dec. 2017.

[12] M. Khalily, R. Tafazolli, P. Xiao, and A. A. Kishk, "Broadband mm-wave microstrip array antenna with improved radiation characteristics for different 5G applications," *IEEE Trans. Antennas Propag.*, vol. 66, no. 9, pp. 4641–4647, Sep. 2018.

[13] J. Xu, W. Hong, Z. H. Jiang, H. Zhang, and K. Wu, "Low-profile wideband vertically folded slotted circular patch array for Ka-band applications," *IEEE Trans. Antennas Propag.*, vol. 68, no. 9, pp. 6844–6849, Sep. 2020.

[14] Y. Q. Guo, Y. M. Pan, and S. Y. Zheng, "Design of series-fed, single-layer, and wideband millimeter-wave microstrip arrays," *IEEE Trans. Antennas Propag.*, vol. 68, no. 10, pp. 7017–7026, Oct. 2020.

[15] Z. Guo and Z. Hao, "A compact wideband millimeter-wave substrate-integrated double-line slot array antenna," *IEEE Trans. Antennas Propag.*, vol. 69, no. 2, pp. 882–891, Feb. 2021.

[16] K. Fan, Z. Hao, and Q. Yuan, "A low-profile wideband substrate-integrated waveguide cavity-backed E-shaped patch antenna for the *Q*-LINKPAN applications," *IEEE Trans. Antennas Propag.*, vol. 65, no. 11, pp. 5667–5676, Nov. 2017.

[17] J. Yin, Q. Wu, C. Yu, H. Wang, and W. Hong, "Broadband symmetrical E-shaped patch antenna with multimode resonance for 5G millimeter-wave applications," *IEEE Trans. Antennas Propag.*, vol. 67, no. 7, pp. 4474–4483, Jul. 2019.

[18] T. Zhang, L. Chen, A. U. Zaman, and J. Yang, "Ultra-wideband millimeter-wave planar array antenna with an upside-down structure of printed ridge gap waveguide for stable performance and high antenna efficiency," *IEEE Antennas Wireless Propag. Lett.*, vol. 20, no. 9, pp. 1721–1725, Sep. 2021.

[19] G. Sun and H. Wong, "C-shaped open slot antenna array for millimeter-wave applications," *IEEE Trans. Antennas Propag.*, vol. 69, no. 12, pp. 8426–8435, Dec. 2021.

[20] M. Wang, Q. Zhu, and C. H. Chan, "Wideband, low-profile slot-fed dipole-patch antenna and array," *IEEE Antennas Wireless Propag. Lett.*, vol. 19, no. 12, pp. 2250–2254, Dec. 2020.

[21] M. Wang and C. H. Chan, "Dual-polarized, low-profile dipole-patch array for wide bandwidth applications," *IEEE Trans. Antennas Propag.*, vol. 70, no. 9, pp. 8030–8039, Sep. 2022.

[22] T. Li and Z. N. Chen, "Wideband substrate-integrated waveguide-fed endfire metasurface antenna array," *IEEE Trans. Antennas Propag.*, vol. 66, no. 12, pp. 7032–7040, Dec. 2018.

[23] T. Li and Z. N. Chen, "Wideband sidelobe-level reduced Ka-band metasurface antenna array fed by substrate-integrated gap waveguide using characteristic mode analysis," *IEEE Trans. Antennas Propag.*, vol. 68, no. 3, pp. 1356–1365, Mar. 2020.

[24] K. B. Ng, H. Wong, K. K. So, C. H. Chan, and K. M. Luk, "60 GHz plated through hole printed magneto-electric dipole antenna," *IEEE Trans. Antennas Propag.*, vol. 60, no. 7, pp. 3129–3136, Jul. 2012.

[25] Y. Li, C. Wang, and Y. X. Guo, "A Ka-band wideband dual-polarized magnetoelectric dipole antenna array on LTCC," *IEEE Trans. Antennas Propag.*, vol. 68, no. 6, pp. 4985–4990, Jun. 2020.

[26] J. Yin, Q. Wu, C. Yu, H. Wang, and W. Hong, "Broadband endfire magnetoelectric dipole antenna array using SICL feeding network for 5G millimeter-wave applications," *IEEE Trans. Antennas Propag.*, vol. 67, no. 7, pp. 4895–4900, Jul. 2019.

[27] J. Xu, W. Hong, Z. H. Jiang, and H. Zhang, "Millimeter-wave broadband substrate integrated magneto-electric dipole arrays with corporate low-profile microstrip feeding structures," *IEEE Trans. Antennas Propag.*, vol. 68, no. 10, pp. 7056–7067, Oct. 2020.

[28] J. Sun, A. Li, and K. Luk, "A high-gain millimeter-wave magnetoelectric dipole array with packaged microstrip line feed network," *IEEE Antennas Wireless Propag. Lett.*, vol. 19, no. 10, pp. 1669–1673, Oct. 2020.

[29] X. Dai, A. Li, and K. M. Luk, "A wideband compact magnetoelectric dipole antenna fed by SICL for millimeter wave applications," *IEEE Trans. Antennas Propag.*, vol. 69, no. 9, pp. 5278–5285, Sep. 2021.

[30] N. Zhang, Z. Yue, Y. Liu, Z. Xue, and Y. Jia, "A wideband low-profile millimeter-wave magneto-electric dipole-like array with low transmission loss feed network," *IEEE Antennas Wireless Propag. Lett.*, vol. 21, no. 2, pp. 277–281, Feb. 2022.

[31] Y. Cui, R. Li, and P. Wang, "A novel broadband planar antenna for 2G/3G/LTE base stations," *IEEE Trans. Antennas Propag.*, vol. 61, no. 5, pp. 2767–2774, May 2013.